

---

*This copy is for your personal, non-commercial use only.*

---

**If you wish to distribute this article to others**, you can order high-quality copies for your colleagues, clients, or customers by [clicking here](#).

**Permission to republish or repurpose articles or portions of articles** can be obtained by following the guidelines [here](#).

**The following resources related to this article are available online at [www.sciencemag.org](http://www.sciencemag.org) (this information is current as of October 20, 2011 ):**

**Updated information and services**, including high-resolution figures, can be found in the online version of this article at:

<http://www.sciencemag.org/content/334/6054/333.full.html>

**Supporting Online Material** can be found at:

<http://www.sciencemag.org/content/suppl/2011/08/31/science.1210713.DC1.html>

This article **cites 31 articles**, 4 of which can be accessed free:

<http://www.sciencemag.org/content/334/6054/333.full.html#ref-list-1>

This article has been **cited by** 1 articles hosted by HighWire Press; see:

<http://www.sciencemag.org/content/334/6054/333.full.html#related-urls>

# Light Propagation with Phase Discontinuities: Generalized Laws of Reflection and Refraction

Nanfang Yu,<sup>1</sup> Patrice Genevet,<sup>1,2</sup> Mikhail A. Kats,<sup>1</sup> Francesco Aieta,<sup>1,3</sup> Jean-Philippe Tetienne,<sup>1,4</sup> Federico Capasso,<sup>1,\*</sup> Zeno Gaburro<sup>1,5\*</sup>

Conventional optical components rely on gradual phase shifts accumulated during light propagation to shape light beams. New degrees of freedom are attained by introducing abrupt phase changes over the scale of the wavelength. A two-dimensional array of optical resonators with spatially varying phase response and subwavelength separation can imprint such phase discontinuities on propagating light as it traverses the interface between two media. Anomalous reflection and refraction phenomena are observed in this regime in optically thin arrays of metallic antennas on silicon with a linear phase variation along the interface, which are in excellent agreement with generalized laws derived from Fermat's principle. Phase discontinuities provide great flexibility in the design of light beams, as illustrated by the generation of optical vortices through use of planar designer metallic interfaces.

The shaping of the wavefront of light with optical components such as lenses and prisms, as well as diffractive elements such as gratings and holograms, relies on **gradual phase changes** accumulated along the optical path. This approach is generalized in transformation optics (1, 2), which uses metamaterials to bend light in unusual ways, achieving such phenomena as negative refraction, subwavelength-focusing, and cloaking (3, 4) and even to explore unusual geometries of space-time in the early universe (5). A new degree of freedom of controlling wavefronts can be attained by introducing **abrupt phase shifts** over the scale of the wavelength along the optical path, with the propagation of light governed by Fermat's principle. The latter states that the trajectory taken between two points A and B by a ray of light is that of the least optical path,  $\int_A^B n(\vec{r}) d\vec{r}$ , where  $n(\vec{r})$  is the local index of refraction, and readily gives the laws of reflection and refraction between two media. In its most general form, Fermat's principle can be stated as the principle of stationary phase (6–8); that is, the derivative of the phase  $\int_A^B d\varphi(\vec{r})$  accumulated along the actual light path will be zero with respect to infinitesimal variations of the path. We show that an abrupt phase shift  $\Phi(\vec{r}_s)$  over the scale of the wavelength can be introduced in the optical path by suitably engineering the interface

between two media;  $\Phi(\vec{r}_s)$  depends on the coordinate  $\vec{r}_s$  along the interface. Then, the total phase shift  $\Phi(\vec{r}_s) + \int_A^B \vec{k} \cdot d\vec{r}$  will be stationary for the actual path that light takes;  $\vec{k}$  is the wave vector of the propagating light. This provides a generalization of the laws of reflection and refraction, which is applicable to a wide range of subwavelength structured interfaces between two media throughout the optical spectrum.

## Generalized laws of reflection and refraction.

The introduction of an abrupt phase shift, denoted as phase discontinuity, at the interface between two media allows us to revisit the laws of reflection and refraction by applying Fermat's principle. Consider an incident plane wave at an angle  $\theta_i$ . Assuming that the two paths are infinitesimally close to the actual light path (Fig. 1), then the phase difference between them is zero

$$[k_0 n_i \sin(\theta_i) dx + (\Phi + d\Phi)] - [k_0 n_t \sin(\theta_t) dx + \Phi] = 0 \quad (1)$$

where  $\theta_t$  is the angle of refraction;  $\Phi$  and  $\Phi + d\Phi$  are, respectively, the phase discontinuities at the locations where the two paths cross the interface;  $dx$  is the distance between the crossing points;  $n_i$  and  $n_t$  are the refractive indices of the two media; and  $k_0 = 2\pi/\lambda_0$ , where  $\lambda_0$  is the vacuum wavelength. If the phase gradient along the interface is designed to be constant, the previous equation leads to the generalized Snell's law of refraction

$$\sin(\theta_t) n_t - \sin(\theta_i) n_i = \frac{\lambda_0}{2\pi} \frac{d\Phi}{dx} \quad (2)$$

Equation 2 implies that the refracted beam can have an arbitrary direction, provided that a suitable constant gradient of phase discontinuity along the interface ( $d\Phi/dx$ ) is introduced. Because of the nonzero phase gradient in this modified Snell's law, the two angles of incidence  $\pm\theta_i$  lead to different values for the angle of refraction. As a consequence, there are two possible critical an-

gles for total internal reflection, provided that  $n_t < n_i$ :

$$\theta_c = \arcsin\left(\pm \frac{n_t}{n_i} - \frac{\lambda_0}{2\pi n_i} \frac{d\Phi}{dx}\right) \quad (3)$$

Similarly, for reflection we have

$$\sin(\theta_r) - \sin(\theta_i) = \frac{\lambda_0}{2\pi n_i} \frac{d\Phi}{dx} \quad (4)$$

where  $\theta_r$  is the angle of reflection. There is a nonlinear relation between  $\theta_r$  and  $\theta_i$ , which is markedly different from conventional specular reflection. Equation 4 predicts that there is always a critical angle of incidence

$$\theta'_c = \arcsin\left(1 - \frac{\lambda_0}{2\pi n_i} \left| \frac{d\Phi}{dx} \right| \right) \quad (5)$$

above which the reflected beam becomes evanescent.

In the above derivation, we have assumed that  $\Phi$  is a continuous function of the position along the interface; thus, all the incident energy is transferred into the anomalous reflection and refraction. However, because experimentally we use an array of optically thin resonators with subwavelength separation to achieve the phase change along the interface, this discreteness implies that there are also regularly reflected and refracted beams, which follow conventional laws of reflection and refraction ( $d\Phi/dx = 0$  in Eqs. 2 and 4). The separation between the resonators controls the amount of energy in the anomalously reflected and refracted beams. We have also assumed that the amplitudes of the scattered radiation by each resonator are identical, so that the reflected and refracted beams are plane waves. In the next section, we will show with simulations—which represent numerical solutions of Maxwell's

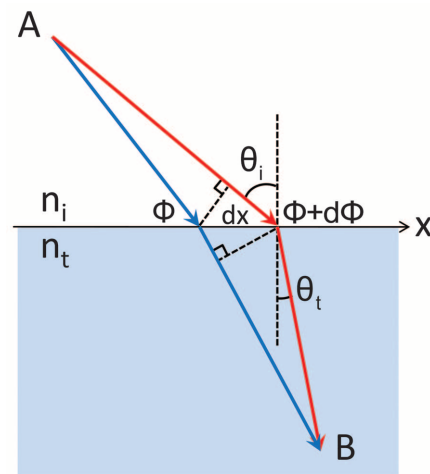


**Fig. 1.** Schematics used to derive the generalized Snell's law of refraction. The interface between the two media is artificially structured in order to introduce an abrupt phase shift in the light path, which is a function of the position along the interface.  $\Phi$  and  $\Phi + d\Phi$  are the phase shifts where the two paths (blue and red) cross the boundary.

<sup>1</sup>School of Engineering and Applied Sciences, Harvard University, Cambridge, MA 02138, USA. <sup>2</sup>Institute for Quantum Studies and Department of Physics, Texas A&M University, College Station, TX 77843, USA. <sup>3</sup>Dipartimento di Fisica e Ingegneria dei Materiali e del Territorio, Università Politecnica delle Marche, via Brecce Bianche, 60131 Ancona, Italy. <sup>4</sup>Laboratoire de Photonique Quantique et Moléculaire, Ecole Normale Supérieure de Cachan and CNRS, 94235 Cachan, France. <sup>5</sup>Dipartimento di Fisica, Università degli Studi di Trento, via Sommarive 14, 38100 Trento, Italy.

\*To whom correspondence should be addressed. E-mail: capasso@seas.harvard.edu (F.C.); gaburro@seas.harvard.edu (Z.G.)

equations—how, indeed, one can achieve the equal-amplitude condition and the constant phase gradient along the interface through suitable design of the resonators.

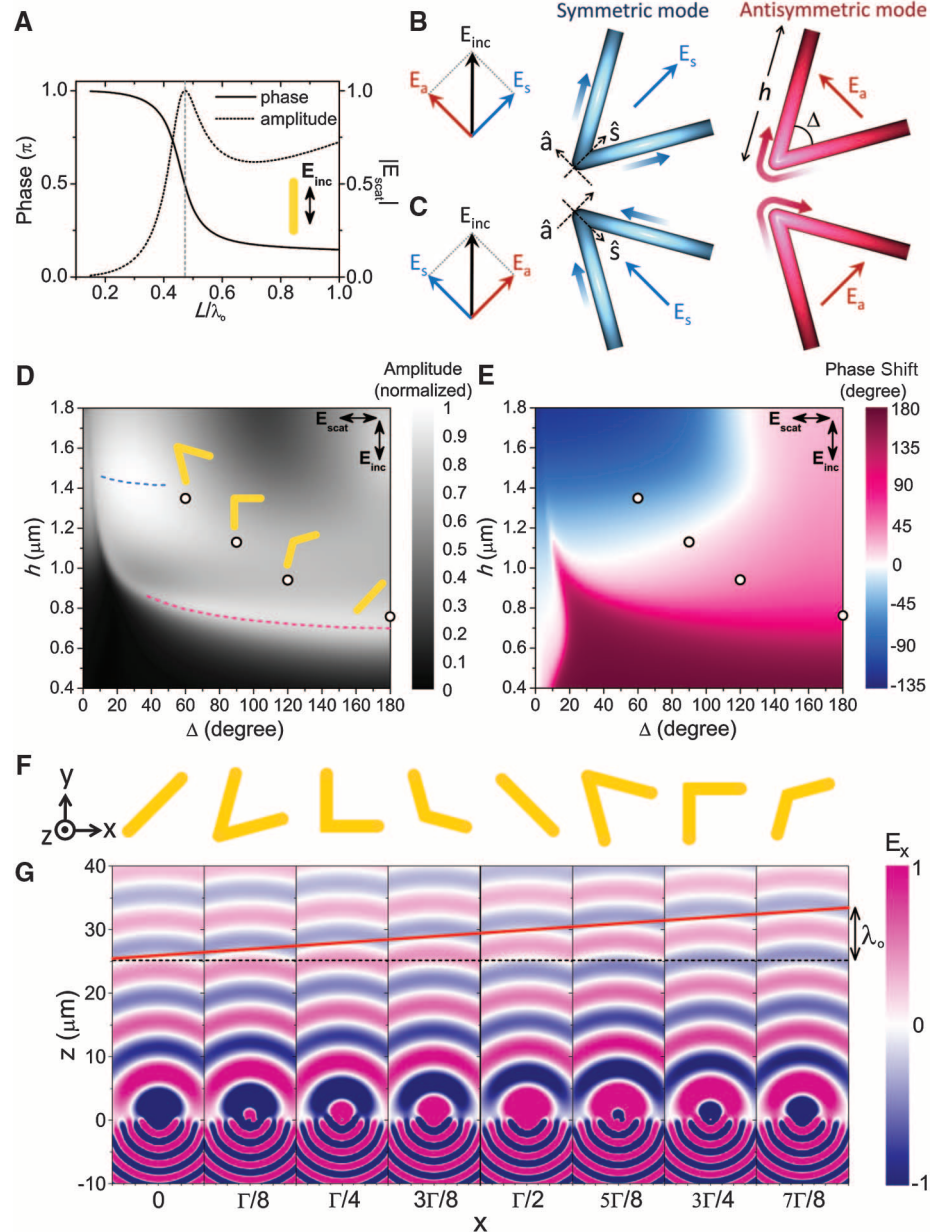
There is a fundamental difference between the anomalous refraction phenomena caused by phase discontinuities and those found in bulk designer metamaterials, which are caused by either negative dielectric permittivity and negative magnetic permeability or anisotropic dielectric permittivity with different signs of permittivity tensor components along and transverse to the surface (3, 4).

**Phase response of optical antennas.** The phase shift between the emitted and the incident radiation of an optical resonator changes appreciably

across a resonance. By spatially tailoring the geometry of the resonators in an array and hence their frequency response, one can design the phase discontinuity along the interface and mold the wavefront of the reflected and refracted beams in nearly arbitrary ways. The choice of the resonators is potentially wide-ranging, from electromagnetic cavities (9, 10) to nanoparticle clusters (11, 12) and plasmonic antennas (13, 14). We concentrated on the latter because of their widely tailorable optical properties (15–19) and the ease of fabricating planar antennas of nanoscale thickness. The resonant nature of a rod antenna made of a perfect electric conductor is shown in Fig. 2A (20).

Phase shifts covering the 0-to- $2\pi$  range are needed to provide full control of the wavefront. To achieve the required phase coverage while maintaining large scattering amplitudes, we used the double-resonance properties of V-shaped antennas, which consist of two arms of equal length  $h$  connected at one end at an angle  $\Delta$  (Fig. 2B). We define two unit vectors to describe the orientation of a V-antenna:  $\hat{s}$  along the symmetry axis of the antenna and  $\hat{a}$  perpendicular to  $\hat{s}$  (Fig. 2B). V-antennas support “symmetric” and “antisymmetric” modes (Fig. 2B, middle and right), which are excited by electric-field components along  $\hat{s}$  and  $\hat{a}$  axes, respectively. In the symmetric mode, the current distribution in each arm approximates

**Fig. 2. (A)** Calculated phase and amplitude of scattered light from a straight rod antenna made of a perfect electric conductor (20). The vertical dashed line indicates the first-order dipolar resonance of the antenna. **(B)** A V-antenna supports symmetric and antisymmetric modes, which are excited, respectively, by components of the incident field along  $\hat{s}$  and  $\hat{a}$  axes. The angle between the incident polarization and the antenna symmetry axis is  $45^\circ$ . The schematic current distribution is represented by colors on the antenna (blue for symmetric and red for antisymmetric mode), with brighter color representing larger currents. The direction of current flow is indicated by arrows with color gradient. **(C)** V-antennas corresponding to mirror images of those in (B). The components of the scattered electric field perpendicular to the incident field in (B) and (C) have a  $\pi$  phase difference. **(D)** and **(E)** Analytically calculated amplitude and phase shift of the cross-polarized scattered light for V-antennas consisting of gold rods with a circular cross section and with various length  $h$  and angle between the rods  $\Delta$  at  $\lambda_0 = 8 \mu\text{m}$  (20). The four circles in (D) and (E) indicate the values of  $h$  and  $\Delta$  used in experiments. The rod geometry enables analytical calculations of the phase and amplitude of the scattered light, without requiring the extensive numerical simulations needed to compute the same quantities for “flat” antennas with a rectangular cross-section, as used in the experiments. The optical properties of a rod and “flat” antenna of the same length are quantitatively very similar, when the rod antenna diameter and the “flat” antenna width and thickness are much smaller than the length (20). **(F)** Schematic unit cell of the plasmonic interface for demonstrating the generalized laws of reflection and refraction. The sample shown in Fig. 3A is created by periodically translating in the  $x$ - $y$  plane the unit cell. The antennas are designed to have equal scattering amplitudes and constant phase difference  $\Delta\Phi = \pi/4$  between neighbors. **(G)** Finite-difference time-domain (FDTD) simulations of the scattered electric field for the individual antennas composing the array in (F). Plots show the scattered electric field polarized in the  $x$  direction for  $y$ -polarized plane wave excitation at normal incidence from the silicon substrate. The silicon substrate is located at  $z \leq 0$ . The antennas are equally spaced at a sub-wavelength separation  $\Gamma/8$ , where  $\Gamma$  is the unit cell length. The tilted red straight line in (G) is the envelope of the projections of the spherical waves scattered by the antennas onto the  $x$ - $z$  plane. On account of Huygens’s



principle, the anomalously refracted beam resulting from the superposition of these spherical waves is then a plane wave that satisfies the generalized Snell’s law (Eq. 2) with a phase gradient  $|d\Phi/dx| = 2\pi/\Gamma$  along the interface.



that of an individual straight antenna of length  $h$  (Fig. 2B, middle), and therefore the first-order antenna resonance occurs at  $h \approx \lambda_{\text{eff}}/2$ , where  $\lambda_{\text{eff}}$  is the effective wavelength (14). In the anti-symmetric mode, the current distribution in each arm approximates that of one half of a straight antenna of length  $2h$  (Fig. 2B, right), and the condition for the first-order resonance of this mode is  $2h \approx \lambda_{\text{eff}}/2$ .

The polarization of the scattered radiation is the same as that of the incident light when the latter is polarized along  $\hat{s}$  or  $\hat{a}$ . For an arbitrary incident polarization, both antenna modes are excited but with substantially different amplitude and phase because of their distinctive resonance conditions. As a result, the scattered light can have a polarization different from that of the incident light. These modal properties of the V-antennas allow one to design the amplitude, phase, and polarization state of the scattered light. We chose the incident polarization to be at  $45^\circ$  with respect to  $\hat{s}$  and  $\hat{a}$  so that both the symmetric and antisymmetric modes can be excited and the scattered light has a substantial component polarized orthogonal to that of the incident light. Experimentally, this allows us to use a polarizer to decouple the scattered light from the excitation.

As a result of the modal properties of the V-antennas and the degrees of freedom in choosing antenna geometry ( $h$  and  $\Delta$ ), the cross-polarized scattered light can have a large range of phases and amplitudes for a given wavelength  $\lambda_0$ ; ana-

lytical calculations of the amplitude and phase response of V-antennas assumed to be made of gold rods are shown in Fig. 2, D and E. In Fig. 2D, the blue and red dashed curves correspond to the resonance peaks of the symmetric and anti-symmetric modes, respectively. We chose four antennas detuned from the resonance peaks, as indicated by circles in Fig. 2, D and E, which provide an incremental phase of  $\pi/4$  from left to right for the cross-polarized scattered light. By simply taking the mirror structure (Fig. 2C) of an existing V-antenna (Fig. 2B), one creates a new antenna whose cross-polarized radiation has an additional  $\pi$  phase shift. This is evident by observing that the currents leading to cross-polarized radiation are  $\pi$  out of phase in Fig. 2, B and C. A set of eight antennas were thus created from the initial four antennas, as shown in Fig. 2F. Full-wave simulations confirm that the amplitudes of the cross-polarized radiation scattered by the eight antennas are nearly equal, with phases in  $\pi/4$  increments (Fig. 2G).

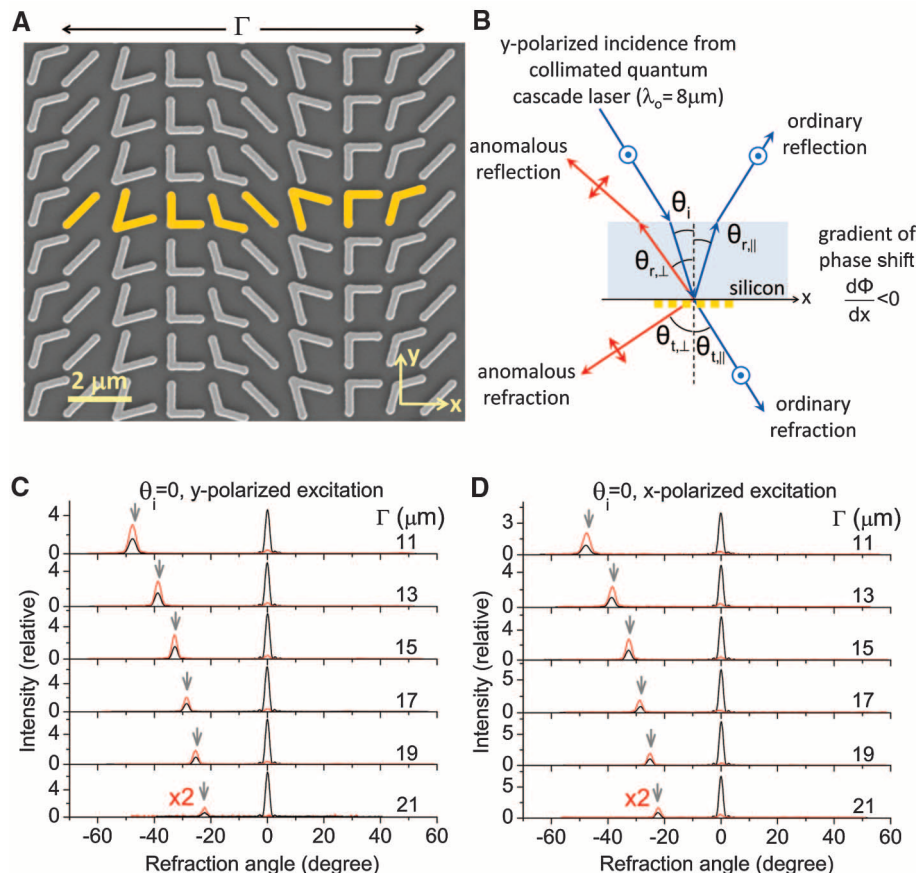
A large phase coverage ( $\sim 300^\circ$ ) can also be achieved by using arrays of straight antennas (fig. S3). However, to obtain the same range of phase shift their scattering amplitudes will be substantially smaller than those of V-antennas (fig. S3). As a consequence of its double resonances, the V-antenna instead allows one to design an array with phase coverage of  $2\pi$  and equal, yet high, scattering amplitudes for all of the array elements, leading to anomalously reflected and refracted beams of substantially higher intensities.

**Experiments on anomalous reflection and refraction.** We demonstrated experimentally the generalized laws of reflection and refraction using plasmonic interfaces constructed by periodically arranging the eight constituent antennas as explained in the caption of Fig. 2F. The spacing between the antennas should be subwavelength so as to provide efficient scattering and to prevent the occurrence of grating diffraction. However, it should not be too small; otherwise, the strong near-field coupling between neighboring antennas would perturb the designed scattering amplitudes and phases. A representative sample with the densest packing of antennas,  $\Gamma = 11 \mu\text{m}$ , is shown in Fig. 3A, where  $\Gamma$  is the lateral period of the antenna array. In the schematic of the experimental setup (Fig. 3B), we assume that the cross-polarized scattered light from the antennas on the left side is phase-delayed as compared with the ones on the right. By substituting into Eq. 2  $-2\pi/\Gamma$  for  $d\Phi/dx$  and the refractive indices of silicon and air ( $n_{\text{Si}}$  and 1) for  $n_i$  and  $n_t$ , we obtain the angle of refraction for the cross-polarized beam

$$\theta_{t,\perp} = \arcsin[n_{\text{Si}} \sin(\theta_i) - \lambda_0/\Gamma] \quad (6)$$

Figure 3C summarizes the experimental results of the ordinary and the anomalous refraction for six samples with different  $\Gamma$  at normal incidence. The incident polarization is along the  $y$  axis in Fig. 3A. The sample with the smallest  $\Gamma$  corresponds to the largest phase gradient and the most

**Fig. 3. (A)** Scanning electron microscope (SEM) image of a representative antenna array fabricated on a silicon wafer. The unit cell of the plasmonic interface (yellow) comprises eight gold V-antennas of width  $\sim 220$  nm and thickness  $\sim 50$  nm, and it repeats with a periodicity of  $\Gamma = 11 \mu\text{m}$  in the  $x$  direction and  $1.5 \mu\text{m}$  in the  $y$  direction. **(B)** Schematic experimental setup for  $y$ -polarized excitation (electric field normal to the plane of incidence). **(C and D)** Measured far-field intensity profiles of the refracted beams for  $y$ - and  $x$ -polarized excitations, respectively. The refraction angle is counted from the normal to the surface. The red and black curves are measured with and without a polarizer, respectively, for six samples with different  $\Gamma$ . The polarizer is used to select the anomalously refracted beams that are cross-polarized with respect to the excitation. The amplitude of the red curves is magnified by a factor of two for clarity. The gray arrows indicate the calculated angles of anomalous refraction according to Eq. 6.



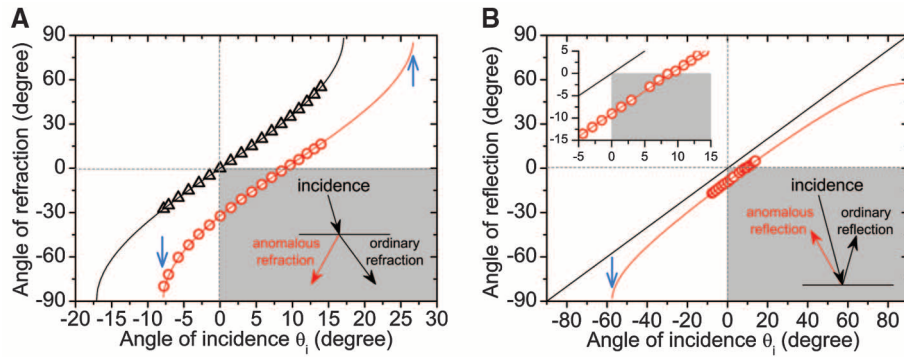
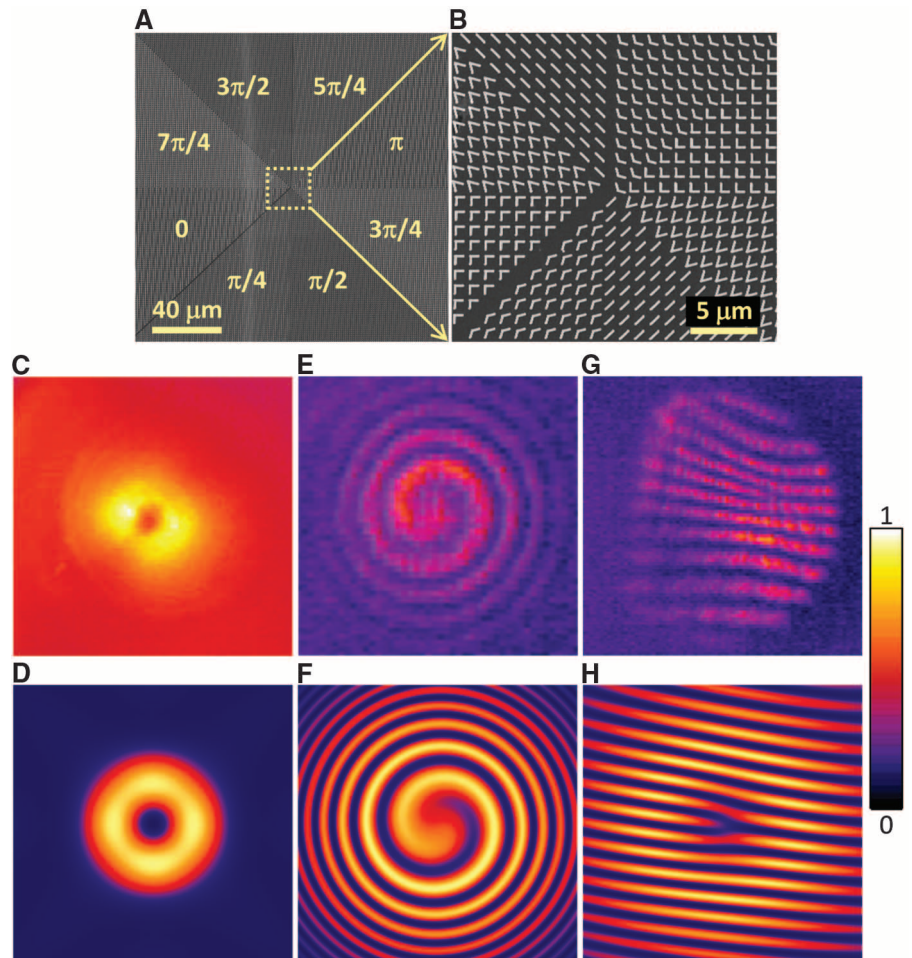


**Fig. 4.** (A) Angle of refraction versus angle of incidence for the ordinary (black curve and triangles) and anomalous refraction (red curve and dots) for the sample with  $\Gamma = 15 \mu\text{m}$ . The curves are theoretical calculations made by using the generalized Snell's law for refraction (Eq. 2), and the symbols are experimental data extracted from refraction measurements as a function of the angle of incidence (20). The shaded blue region represents "negative" refraction for the cross-polarized light, as illustrated in the inset. The blue arrows indicate the modified critical angles for total internal reflection. (B) Angle of reflection versus angle of incidence for the ordinary (black curve) and anomalous (red curve and dots) reflection for the sample with  $\Gamma = 15 \mu\text{m}$ . The top left inset is the zoom-in view. The curves are theoretical calculations made by using Eq. 4, and the symbols are experimental data extracted from reflection measurements as a function of the angle of incidence (20). The shaded region represents "negative" reflection for the cross-polarized light, as illustrated in the bottom right inset. The blue arrow indicates the critical angle of incidence above which the anomalously reflected beam becomes evanescent. Experiments with lasers emitting at different wavelengths show that the plasmonic interfaces are broadband, anomalously reflecting and refracting light from  $\lambda \approx 5 \mu\text{m}$  to  $\lambda \approx 10 \mu\text{m}$ .

**Fig. 5.** (A) SEM image of a plasmonic interface that creates an optical vortex. The plasmonic pattern consists of eight regions, each occupied by one constituent antenna of the eight-element set of Fig. 2F. The antennas are arranged so as to generate a phase shift that varies azimuthally from 0 to  $2\pi$ , thus producing a helicoidal scattered wavefront. (B) Zoom-in view of the center part of (A). (C and D) Respectively, measured and calculated far-field intensity distributions of an optical vortex with topological charge one. The constant background in (C) is due to the thermal radiation. (E and F) Respectively, measured and calculated spiral patterns created by the interference of the vortex beam and a co-propagating Gaussian beam. (G and H) Respectively, measured and calculated interference patterns with a dislocated fringe created by the interference of the vortex beam and a Gaussian beam when the two are tilted with respect to each other. The circular border of the interference pattern in (G) arises from the finite aperture of the beam splitter used to combine the vortex and the Gaussian beams (20). The size of (C) and (D) is 60 mm by 60 mm, and that of (E) to (H) is 30 mm by 30 mm.



efficient light scattering into the cross-polarized beams. We observed that the angles of anomalous refraction agree well with theoretical predictions of Eq. 6 (Fig. 3C). The same peak positions were observed for normal incidence, with polarization along the  $x$  axis in Fig. 3A (Fig. 3D). To a good approximation, we expect that the V-antennas were operating independently at the packing density used in experiments (20). The purpose of using a large antenna array ( $\sim 230 \mu\text{m}$  by  $230 \mu\text{m}$ ) is solely to accommodate the size of the plane-wave-like excitation (beam radius  $\sim 100 \mu\text{m}$ ). The periodic antenna arrangement is used here for convenience but is not necessary to satisfy the generalized laws of reflection and refraction. It is only necessary that the phase gradient is constant along the plasmonic interface and that the scattering amplitudes of the antennas are all equal. The phase increments between nearest neighbors do not need to be constant, if one relaxes the unnecessary constraint of equal spacing between nearest antennas.

The angles of refraction and reflection are shown in Fig. 4, A and B, respectively, as a function of  $\theta_i$  for both the silicon-air interface (black curves and symbols) and the plasmonic interface (red curves and symbols) (20). In the range of  $\theta_i = 0^\circ$  to  $9^\circ$ , the plasmonic interface



exhibits “negative” refraction and reflection for the cross-polarized scattered light (schematics are shown in the bottom right insets of Fig. 4, A and B). The critical angle for total internal reflection is modified to  $\sim -8^\circ$  and  $+27^\circ$  (Fig. 4A, blue arrows) for the plasmonic interface in accordance with Eq. 3, compared with  $\pm 17^\circ$  for the silicon-air interface; the anomalous reflection does not exist beyond  $\theta_i = -57^\circ$  (Fig. 4B, blue arrow).

At normal incidence, the ratio of intensity  $R$  between the anomalously and ordinarily refracted beams is  $\sim 0.32$  for the sample with  $\Gamma = 15 \mu\text{m}$  (Fig. 3C).  $R$  rises for increasing antenna packing densities (Fig. 3, C and D) and increasing angles of incidence [up to  $R \approx 0.97$  at  $\theta_i = 14^\circ$  (fig. S1B)]. Because of the experimental configuration, we are not able to determine the ratio of intensity between the reflected beams (20), but we expect comparable values.

#### Vortex beams created by plasmonic interfaces.

To demonstrate the versatility of the concept of interfacial phase discontinuities, we fabricated a plasmonic interface that is able to create a vortex beam (21, 22) upon illumination by normally incident linearly polarized light. A vortex beam has a helicoidal (or “corkscrew-shaped”) equal-phase wavefront. Specifically, the beam has an azimuthal phase dependence  $\exp(i\ell\varphi)$  and carries an orbital angular momentum of  $L = \ell\hbar$  per photon (23). Here, the topological charge  $\ell$  is an integer, indicating the number of twists of the wavefront within one wavelength;  $\varphi$  is the azimuthal angle with respect to the beam axis; and  $\hbar$  is the reduced Planck constant. These peculiar states of light are commonly generated by using a spiral phase plate (24) or a computer-generated hologram (25) and can be used to rotate particles (26) or to encode information in optical communication systems (27).

The plasmonic interface was created by arranging the eight constituent antennas as shown in Fig. 5, A and B. The interface introduces a spiral-like phase shift with respect to the planar wavefront of the incident light, creating a vortex beam with  $\ell = 1$ . The vortex beam has an annular intensity distribution in the cross section, as viewed in a mid-infrared camera (Fig. 5C); the dark region at the center corresponds to a phase singularity (22). The spiral wavefront of the vortex beam can be revealed by interfering the beam with a co-propagating Gaussian beam (25), producing a spiral interference pattern (Fig. 5E). The latter rotates when the path length of the Gaussian beam was changed continuously relative to that of the vortex beam (movie S1). Alternatively, the topological charge  $\ell = 1$  can be identified by a dislocated interference fringe when the vortex and Gaussian beams interfere with a small angle (Fig. 5G) (25). The annular intensity distribution and the interference patterns were well reproduced in simulations (Fig. 5, D, F, and H) by using the calculated amplitude and phase responses of the V-antennas (Fig. 2, D and E).

**Concluding remarks.** Our plasmonic interfaces, consisting of an array of V-antennas, im-

part abrupt phase shifts in the optical path, thus providing great flexibility in molding of the optical wavefront. This breaks the constraint of standard optical components, which rely on gradual phase accumulation along the optical path to change the wavefront of propagating light. We have derived and experimentally confirmed generalized reflection and refraction laws and studied a series of intriguing anomalous reflection and refraction phenomena that descend from the latter: arbitrary reflection and refraction angles that depend on the phase gradient along the interface, two different critical angles for total internal reflection that depend on the relative direction of the incident light with respect to the phase gradient, and critical angle for the reflected beam to be evanescent. We have also used a plasmonic interface to generate optical vortices that have a helicoidal wavefront and carry orbital angular momentum, thus demonstrating the power of phase discontinuities as a design tool of complex beams. The design strategies presented in this article allow one to tailor in an almost arbitrary way the phase and amplitude of an optical wavefront, which should have major implications for transformation optics and integrated optics. We expect that a variety of novel planar optical components such as phased antenna arrays in the optical domain, planar lenses, polarization converters, perfect absorbers, and spatial phase modulators will emerge from this approach.

Antenna arrays in the microwave and millimeter-wave regions have been used for the shaping of reflected and transmitted beams in the so-called “reflectarrays” and “transmitarrays” (28–31). These typically consist of a double-layer structure comprising a planar array of antennas and a ground plane (in the case of reflectarrays) or another array (in the case of transmitarrays), separated by a dielectric spacer of finite thickness. Reflectarrays and transmitarrays cannot be treated as a single interface for which one can write down the generalized laws because they rely on both antenna resonances and the propagation of waves in the spacer to achieve the desired phase control. The generalization of the laws of reflection and refraction we present is made possible by the deeply subwavelength thickness of our optical antenna arrays and their associated abrupt phase changes, with no contribution from propagation effects. These generalized laws apply to the whole optical spectrum for suitable designer interfaces and can be a guide for the design of new photonic devices.

#### References and Notes

1. J. B. Pendry, D. Schurig, D. R. Smith, *Science* **312**, 1780 (2006).
2. U. Leonhardt, *Science* **312**, 1777 (2006).
3. W. Cai, V. Shalaev, *Optical Metamaterials: Fundamentals and Applications* (Springer, New York, 2009).
4. N. Engheta, R. W. Ziolkowski, *Metamaterials: Physics and Engineering Explorations* (Wiley-IEEE Press, New York, 2006).
5. I. I. Smolyaninov, E. E. Narimanov, *Phys. Rev. Lett.* **105**, 067402 (2010).
6. S. D. Brorson, H. A. Haus, *J. Opt. Soc. Am. B* **5**, 247 (1988).

7. R. P. Feynman, A. R. Hibbs, *Quantum Mechanics and Path Integrals* (McGraw-Hill, New York, 1965).
8. E. Hecht, *Optics* (Addison Wesley, Boston, ed. 3, 1997).
9. H. T. Miyazaki, Y. Kurokawa, *Appl. Phys. Lett.* **89**, 211126 (2006).
10. D. Fattal, J. Li, Z. Peng, M. Fiorentino, R. G. Beausoleil, *Nat. Photonics* **4**, 466 (2010).
11. J. A. Fan et al., *Science* **328**, 1135 (2010).
12. B. Luk'yanchuk et al., *Nat. Mater.* **9**, 707 (2010).
13. R. D. Grober, R. J. Schoelkopf, D. E. Prober, *Appl. Phys. Lett.* **70**, 1354 (1997).
14. L. Novotny, N. van Hulst, *Nat. Photonics* **5**, 83 (2011).
15. Q. Xu et al., *Nano Lett.* **7**, 2800 (2007).
16. M. Sukharev, J. Sung, K. G. Spears, T. Seideman, *Phys. Rev. B* **76**, 184302 (2007).
17. P. Biagioni, J. S. Huang, L. Duò, M. Finazzi, B. Hecht, *Phys. Rev. Lett.* **102**, 256801 (2009).
18. S. Liu et al., *Opt. Lett.* **34**, 1255 (2009).
19. J. Ginn, D. Shelton, P. Krenz, B. Lail, G. Boreman, *Opt. Express* **18**, 4557 (2010).
20. Materials and methods are available as supporting material on Science Online.
21. J. F. Nye, M. V. Berry, *Proc. R. Soc. London A Math. Phys. Sci.* **336**, 165 (1974).
22. M. Padgett, J. Courtial, L. Allen, *Phys. Today* **57**, 35 (2004).
23. L. Allen, M. W. Beijersbergen, R. J. C. Spreeuw, J. P. Woerdman, *Phys. Rev. A* **45**, 8185 (1992).
24. M. W. Beijersbergen, R. P. C. Coerwinkel, M. Kristensen, J. P. Woerdman, *Opt. Commun.* **112**, 321 (1994).
25. N. R. Heckenberg, R. McDuff, C. P. Smith, A. G. White, *Opt. Lett.* **17**, 221 (1992).
26. H. He, M. E. J. Friese, N. R. Heckenberg, H. Rubinsztein-Dunlop, *Phys. Rev. Lett.* **75**, 826 (1995).
27. G. Gibson et al., *Opt. Express* **12**, 5448 (2004).
28. D. M. Pozar, S. D. Targonski, H. D. Syrigos, *IEEE Trans. Antenn. Propag.* **45**, 287 (1997).
29. J. A. Encinar, *IEEE Trans. Antenn. Propag.* **49**, 1403 (2001).
30. C. G. M. Ryan et al., *IEEE Trans. Antenn. Propag.* **58**, 1486 (2010).
31. P. Padilla, A. Muñoz-Acevedo, M. Sierra-Castañer, M. Sierra-Pérez, *IEEE Trans. Antenn. Propag.* **58**, 2571 (2010).

**Acknowledgments:** The authors acknowledge helpful discussion with J. Lin, R. Blanchard, and A. Belyanin. The authors acknowledge support from the National Science Foundation (NSF), Harvard Nanoscale Science and Engineering Center (NSEC) under contract NSF/PHY 06-46094, and the Center for Nanoscale Systems (CNS) at Harvard University. This work was supported in part by the Defense Advanced Research Projects Agency (DARPA) N/MEMS S&T Fundamentals program under grant N66001-10-1-4008 issued by the Space and Naval Warfare Systems Center Pacific (SPAWAR). Z.G. acknowledges funding from the European Communities Seventh Framework Programme (FP7/2007-2013) under grant agreement P10F-GA-2009-235860. M.A.K. is supported by NSF through a Graduate Research Fellowship. Harvard CNS is a member of the National Nanotechnology Infrastructure Network. The Lumerical (Vancouver, BC, Canada) FDTD simulations in this Research Article were run on the Odyssey cluster supported by the Harvard Faculty of Arts and Sciences Sciences Division Research Computing Group.

#### Supporting Online Material

www.sciencemag.org/cgi/content/full/science.1210713/DC1  
Materials and Methods  
SOM Text  
Figs. S1 to S6  
References (32–39)  
Movie S1

5 July 2011; accepted 19 August 2011  
Published online 1 September 2011;  
10.1126/science.1210713